Supporting information

High Photocurrent in Oligo-thienylenevinylene-Based Small Molecule Solar Cells with 4.9% Solar-to-Electrical Energy Conversion.

Núria F. Montcada [a+], Rocío Domínguez [b+], Beatriz Pelado [b], Pilar de la Cruz [b], Emilio Palomares [a,c*], Fernando Langa [b*].

[a]*Institute of Chemical Research of Catalonia (ICIQ), Avinguda del Països Catalans 16, 43007 Tarragona, Spain. Fax: +34 977 920 823; Tel: +34 977 920 200; E-mail: epalomares@iciq.es*

[b] *Institute for Nanoscience, Nanotechnology and Molecular Materials (INAMOL). University of Castilla-la Mancha, Campus de la Fábrica. 45071. Toledo, Spain.*

[c]*Catalan Institution for Research and Advanced Studies (ICREA), Passeig de Lluis Companys 23, 08010 Barcelona, Spain*

Table of contents

1.- Experimental conditions

Synthetic procedures were carried out under inert argon atmosphere, in dry solvent unless otherwise noted. All reagents and solvents were reagent grade and were used without further purification. Chromatographic purifications were performed using silica gel 60 SDS (particle size 0.040-0.063 mm). Analytical thin-layer chromatography was performed using Merck TLC silica gel 60 F254. ^{1}H NMR spectra were obtained on Bruker TopSpin AV-400 (400 MHz) spectrometer. Chemical shifts are reported in parts per million (ppm) relative to the solvent residual peak ($CDCl_3$, 7.27 ppm). ^{13}C NMR chemical shifts are reported relative to the solvent residual peak ($CDCl_3$, 77.00 ppm). UV-Vis measurements were carried out on a Shimadzu UV 3600 spectrophotometer. For extinction coefficient determination, solutions of different concentration were prepared in CH_2Cl_2, HPLC grade, with absorption between 0.1-1 of absorbance using a 1 cm UV cuvette. The emission measurements were carried out on Cary Eclipse fluorescence spectrophotometer. Mass spectra (MALDI-TOF) were recorded on a VOYAGER DE^{TM} STR mass spectrometer using dithranol as matrix. Melting points are uncorrected. Cyclic voltammetry was performed in o-dichlorobenzene/acetonitrile 4:1 solutions. Tetrabutylammonium perchlorate (0.1 M as supporting electrolyte) were purchased from Acros and used without purification. Solutions were deoxygenated by argon bubbling prior to each experiment which was run under argon atmosphere. Experiments were done in a one-compartment cell equipped with a glassy carbon working electrode (∅ = 2 mm) and a platinum wire counter electrode. An Ag/AgNO3 (0.01 M in the supporting electrolyte) electrode was used as reference and checked against the ferrocene/ferrocenium couple (Fc/Fc^+) before and after each experiment.

The thermogravimetric analysis was performed using a TGA/DSC Linea Excellent instrument by Mettler-Toledo, collected under inert atmosphere of nitrogen, with a rate of 10ºC min^{-1}, and the weight changes were recorded as a function of temperature. The differential scanning calorimetry analysis was performed by a DSC Linea Excellent instrument by Mettler-Toledo, collected under inert atmosphere of nitrogen at a heating rate of 20 K/min and a cooling rate of 10 K/min.

The molecular geometries and frontier molecular orbitals of these new dyes have been optimized by density functional theory (DFT) calculations at the B3LYP/6-31G* level.[1]

[1] Gaussian 03, Revision D.02, Frisch, M. J.; Trucks, G. W.; Schlegel, H. B.; Scuseria, G. E.; Robb, M. A.;

2.- ^{1}H NMR, ^{13}C NMR, IR spectra and MS spectra.

Cheeseman, J. R.; Montgomery Jr., J. A.; Vreven, T.; Kudin, K. N.; Burant, J. C.; Millam, J. M.; Iyengar, S. S.; Tomasi, J.; Barone, V.; Mennucci, B.; Cossi, M.; Scalmani, G.; Rega, N.; Petersson, G. A.; Nakatsuji, H.; Hada, M.; Ehara, M.; Toyota, K.; Fukuda, R.; Hasegawa, J.; Ishida, M.; Nakajima, T.; Honda, Y.; Kitao, O.; Nakai, H.; Klene, M.; Li, X.; Knox, J. E.; Hratchian, H. P.; Cross, J. B.; Bakken, V.; Adamo, C.; Jaramillo, J.; Gomperts, R.; Stratmann, R. E.; Yazyev, O.; Austin, A. J.; Cammi, R.; Pomelli, C.; Ochterski, J. W.; Ayala, P. Y.; Morokuma, K.; Voth, G. A.; Salvador, P.; Dannenberg, J. J.; Zakrzewski, V. G.; Dapprich, S.; Daniels, A. D.; Strain, M. C.; Farkas, O.; Malick, D. K.; Rabuck, A. D.; Raghavachari, K.; Foresman, J. B.; Ortiz, J. V.; Cui, Q.; Baboul, A. G.; Clifford, S.; Cioslowski, J.; Stefanov, B. B.; Liu, G.; Liashenko, A.; Piskorz, P.; Komaromi, I.; Martin, R. L.; Fox, D. J.; Keith, T.; Al-Laham, M. A.; Peng, C. Y.; Nanayakkara, A.; Challacombe, M.; Gill, P. M. W.; Johnson, B.; Chen, W.; Wong, M. W.; Gonzalez, C.; Pople, J. A. Gaussian, Inc., Wallingford CT, 2004.

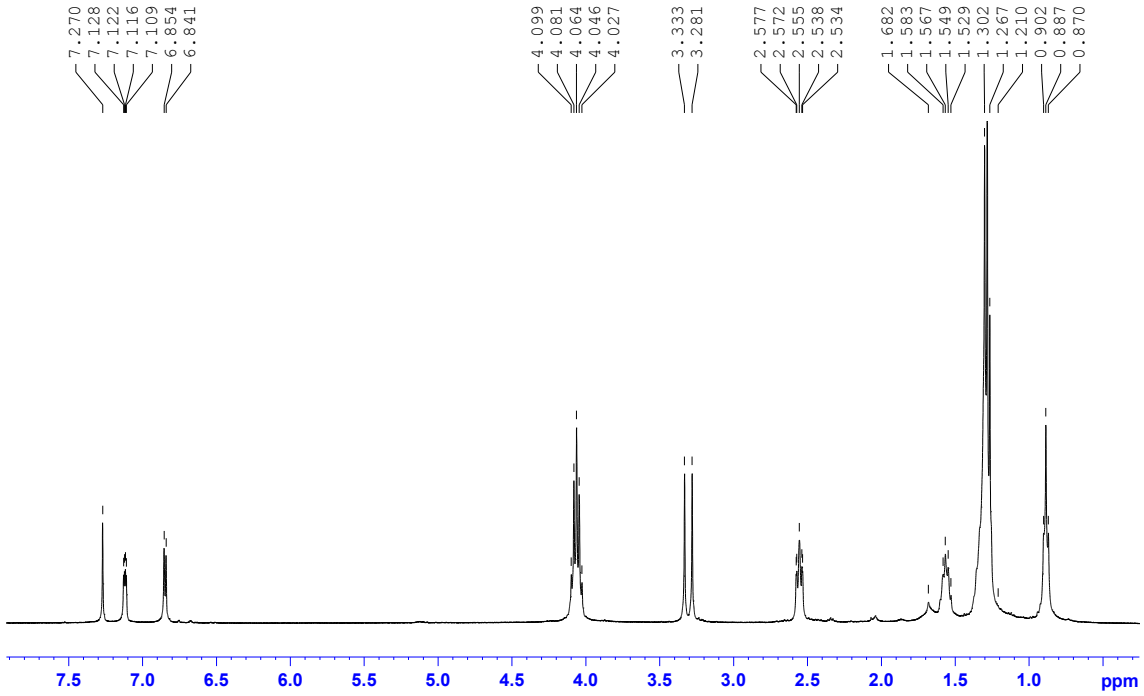

Figure S1. ^{1}H NMR spectrum (400 MHz, $CDCl_3$) of **3**.

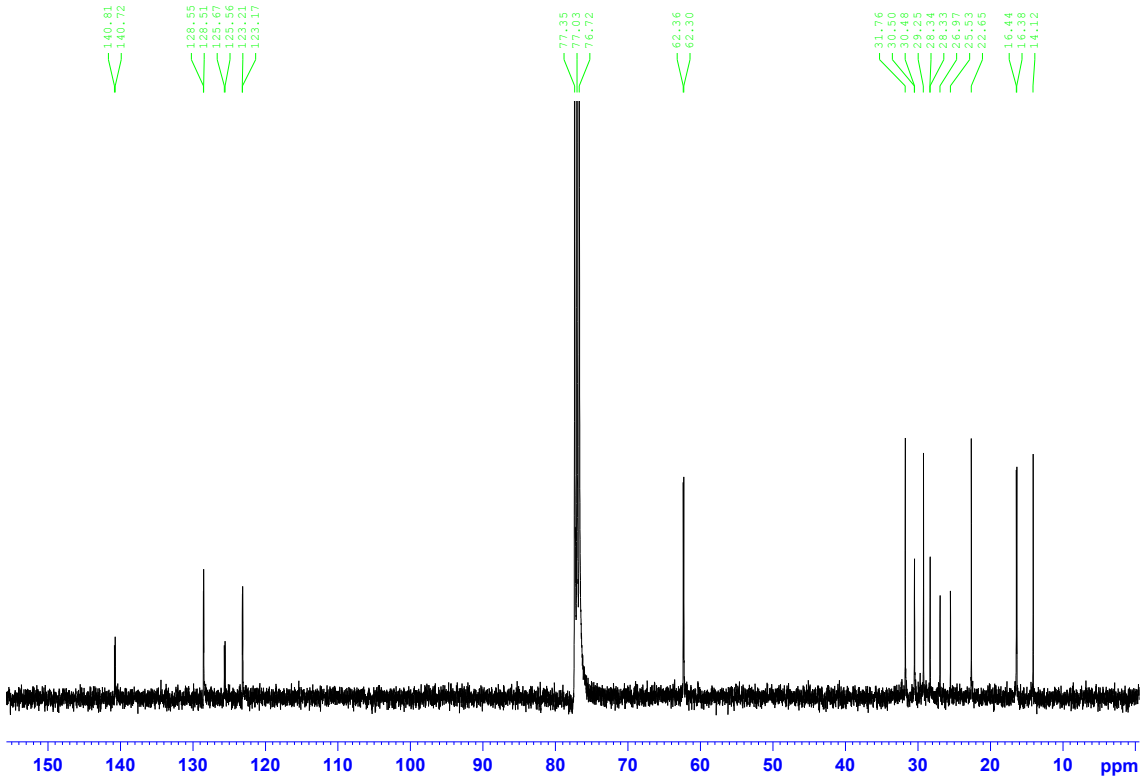

Figure S2. ^{13}C NMR spectrum (100 MHz, $CDCl_3$) of **3**.

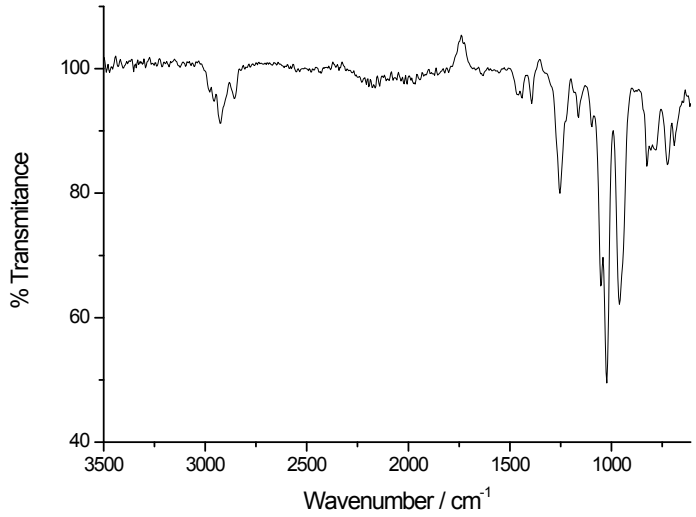

Figure S3. FT-IR spectrum of **3**.

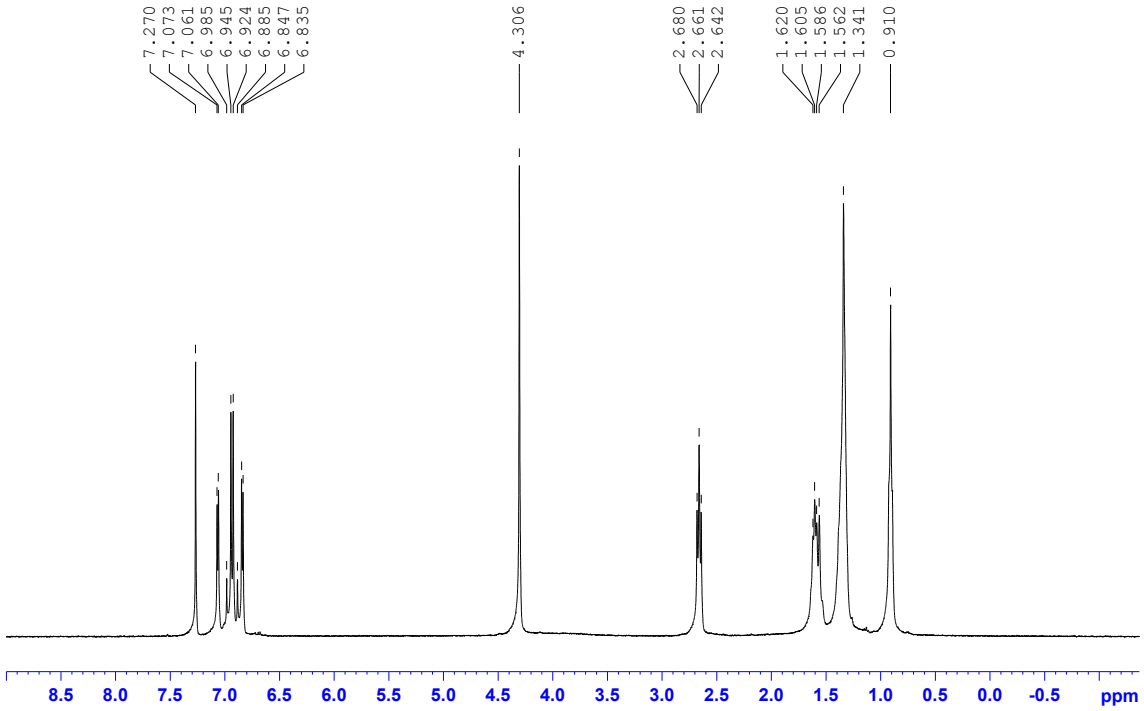

Figure S4. ^{1}H NMR spectrum (400 MHz, $CDCl_3$) of **4**.

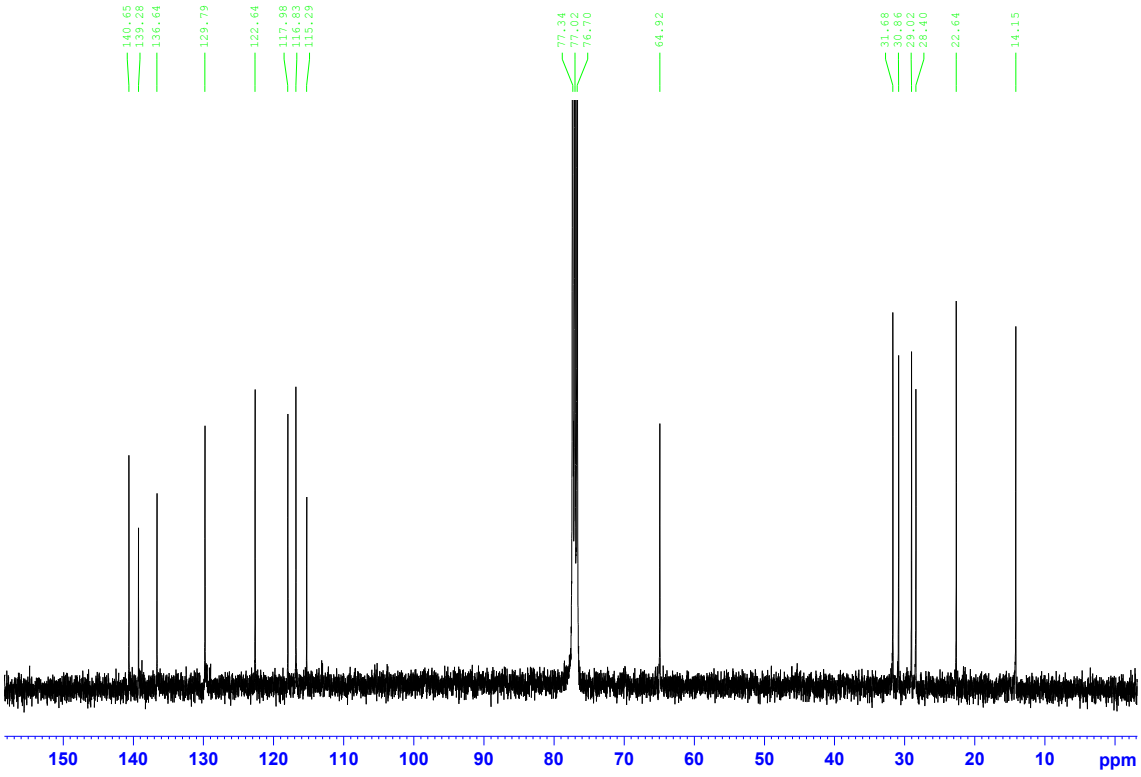

Figure S5. ^{13}C NMR spectrum (100 MHz, $CDCl_3$) of **4**.

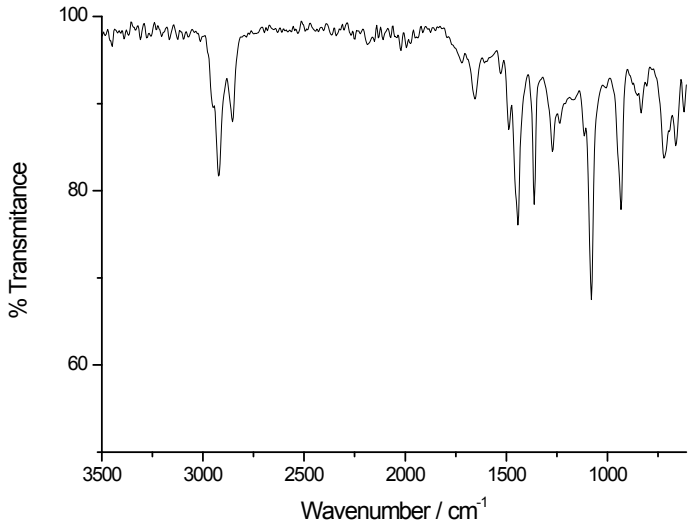

Figure S6. FT-IR spectrum of **4**.

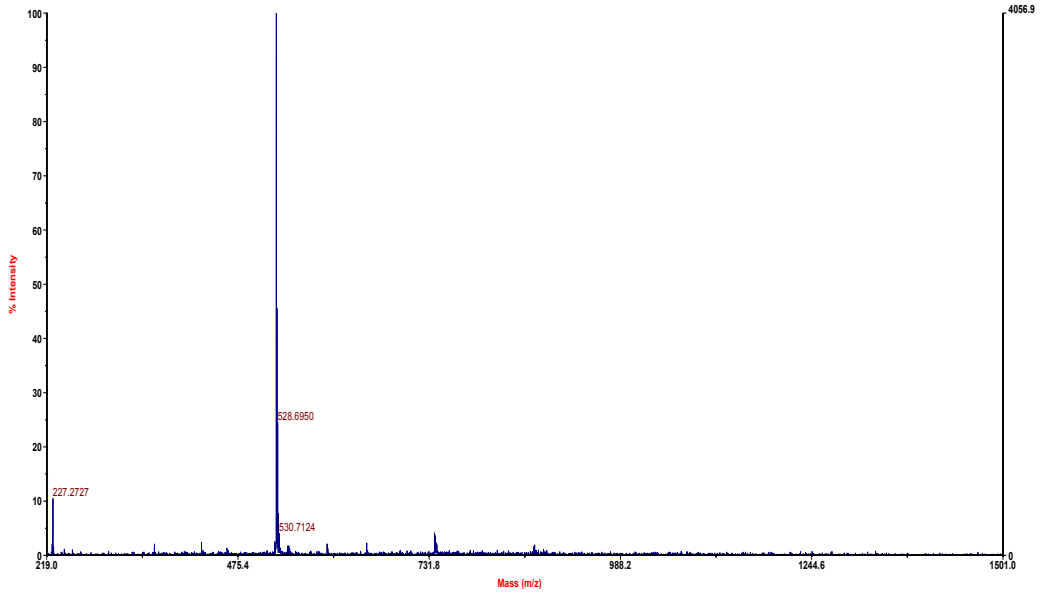

Figure S7. MALDI-MS spectrum of **4** (Matrix: Dithranol).

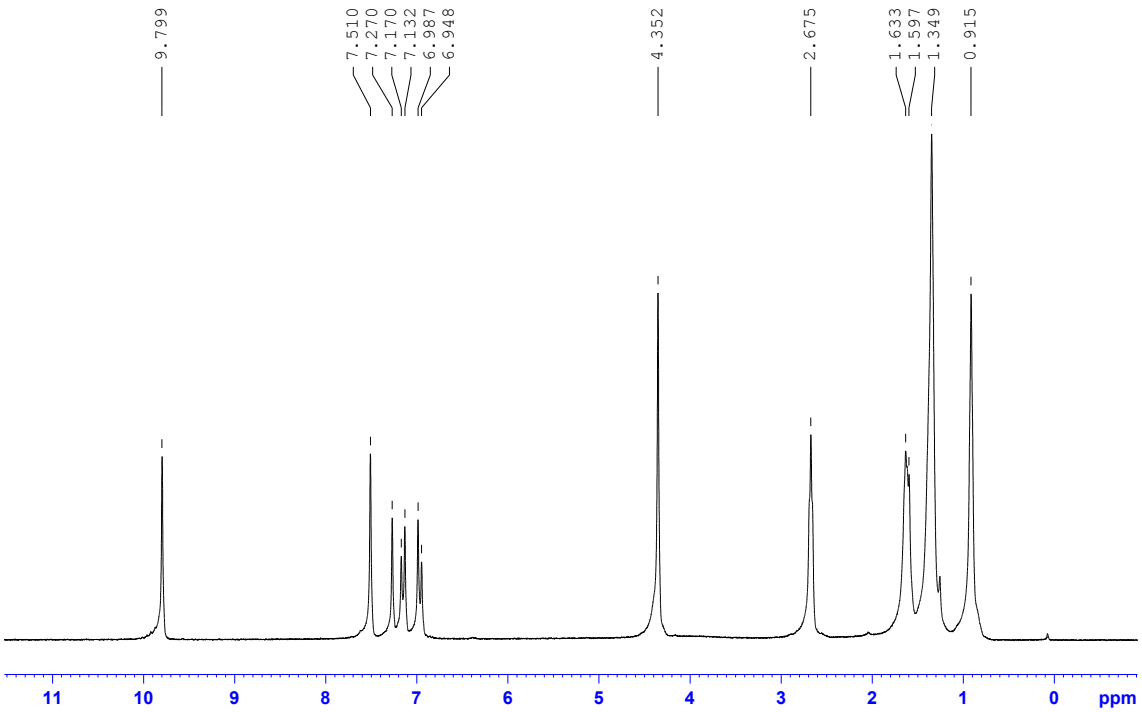

Figure S8. ^{1}H NMR spectrum (400 MHz, $CDCl_3$) of **5a**.

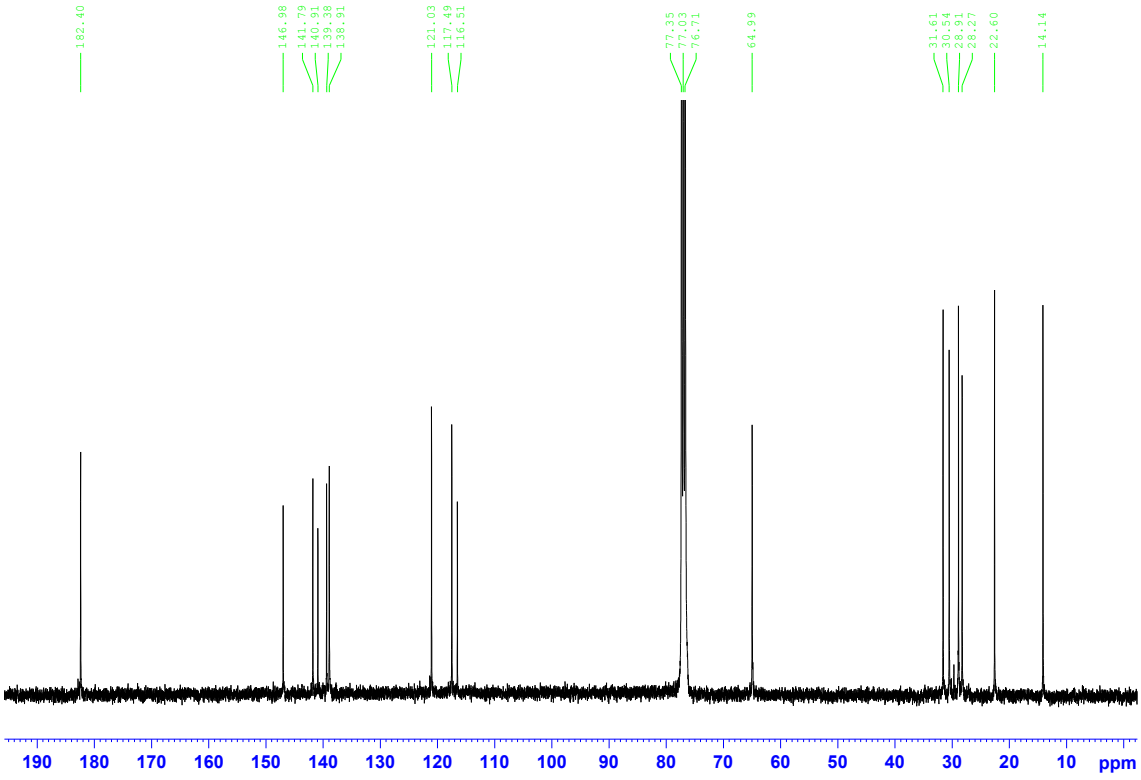

Figure S9. ^{13}C NMR spectrum (100 MHz, $CDCl_3$) of **5a**.

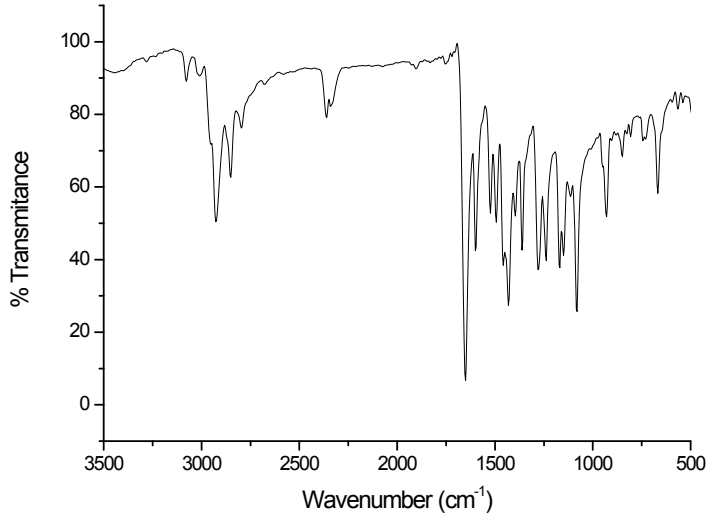

Figure S10. FT-IR spectrum of **5a**.

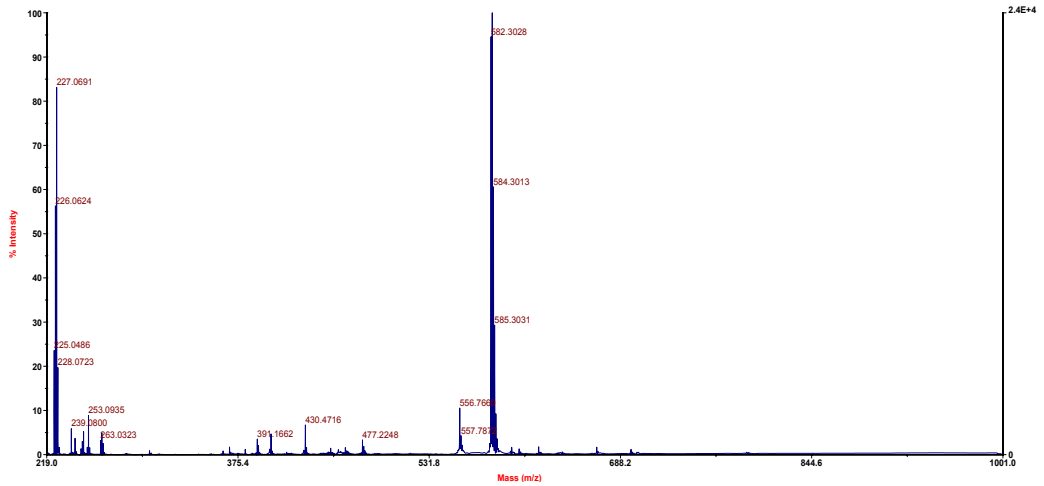

Figure S11. MALDI-MS spectrum of **5a** (Matrix: Dithranol).

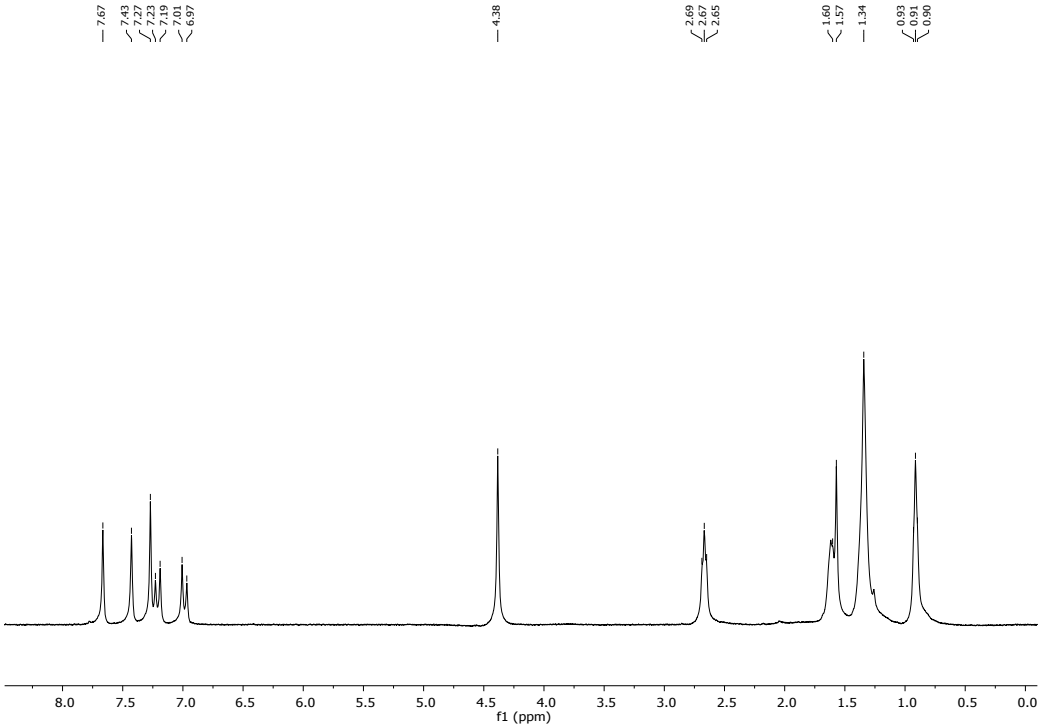

Figure S12. ^{1}H NMR spectrum (400 MHz, $CDCl_3$) of **smL04**.

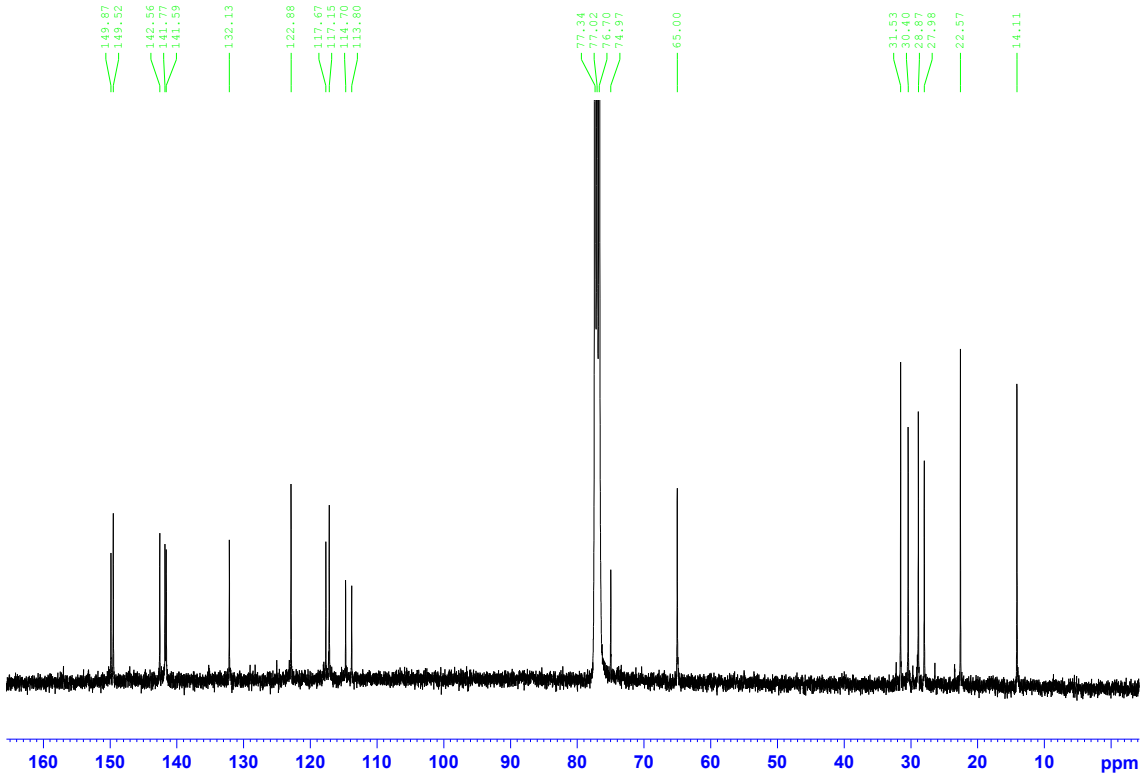

Figure S13. ^{13}C NMR spectrum (100 MHz, $CDCl_3$) of **smL04**.

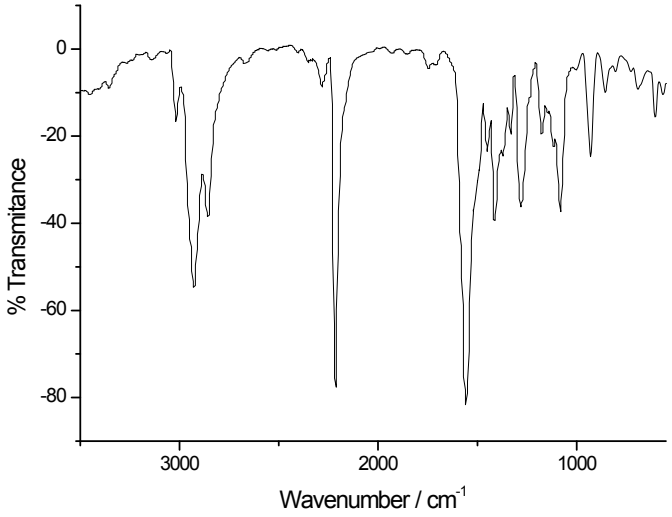

Figure S14. FT-IR spectrum of **smL04.**

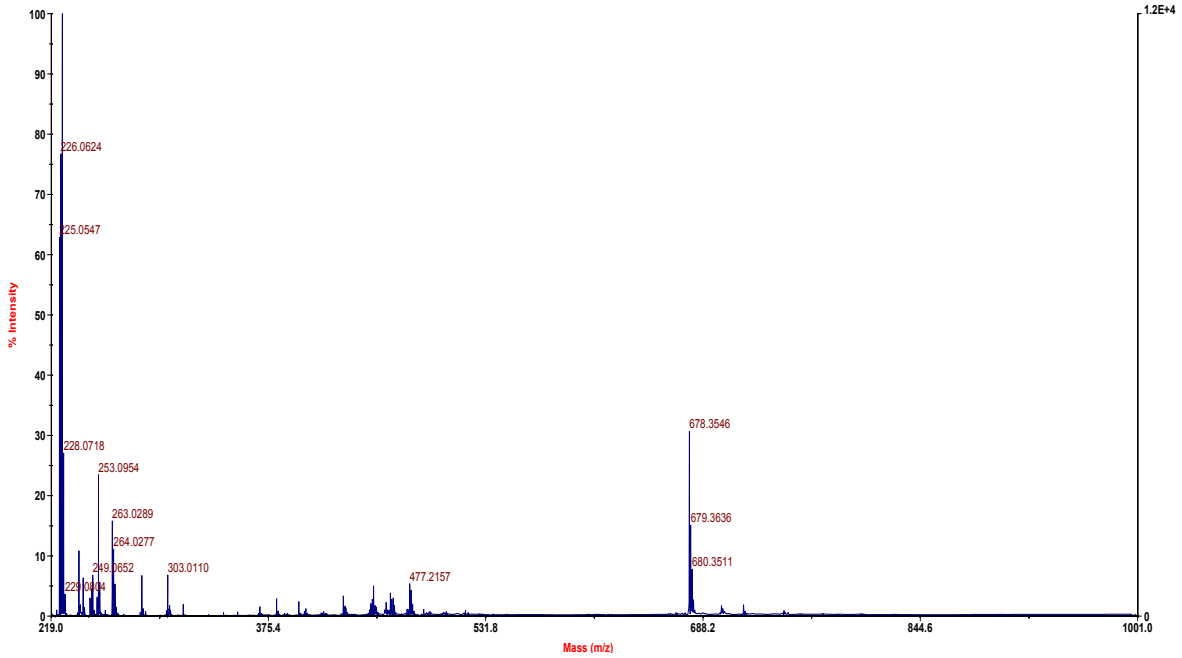

Figure S15. MALDI-MS spectrum of **smL04** (Matrix: Dithranol).

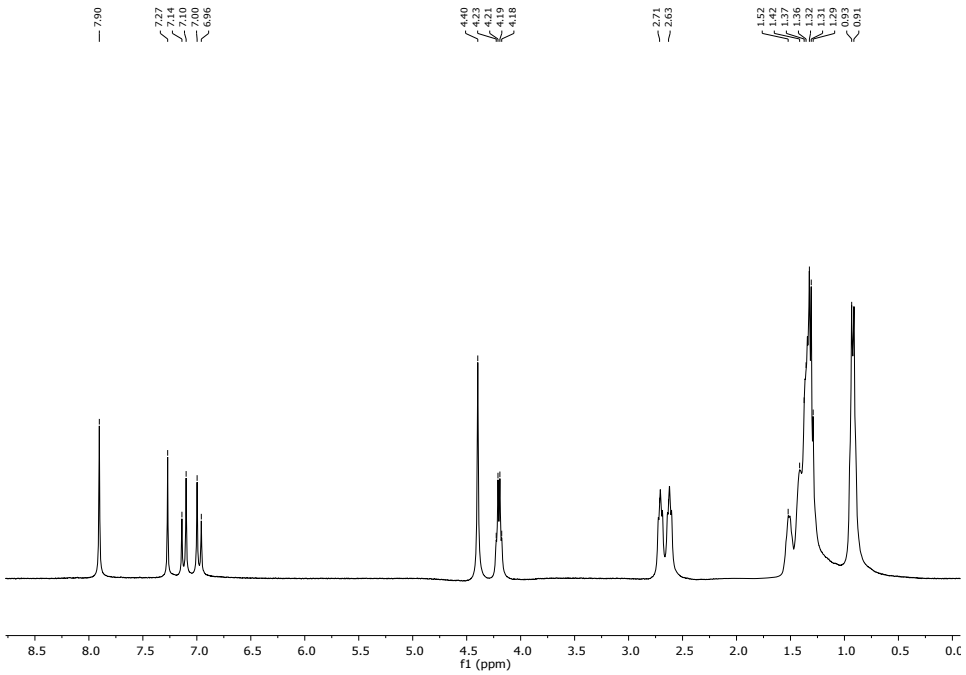

Figure S16. ^{1}H NMR spectrum (400 MHz, $CDCl_3$) of **smL05**.

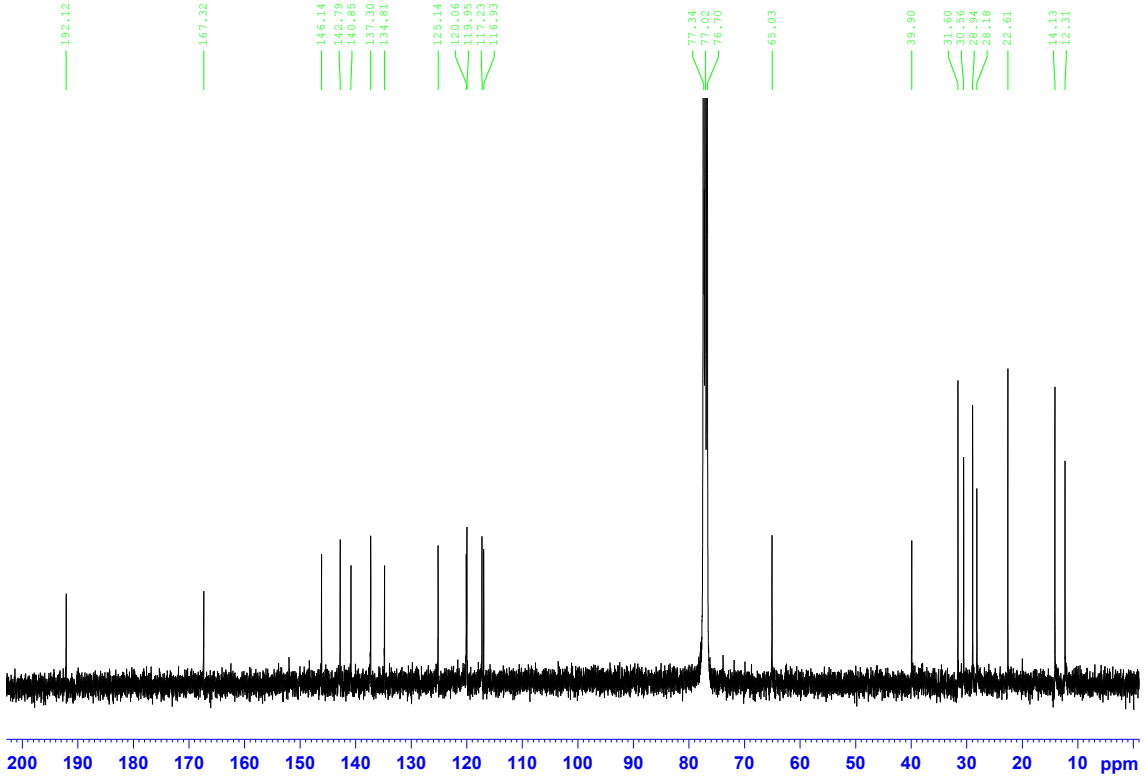

Figure S17. ^{13}C NMR spectrum (100 MHz, $CDCl_3$) of **smL05**.

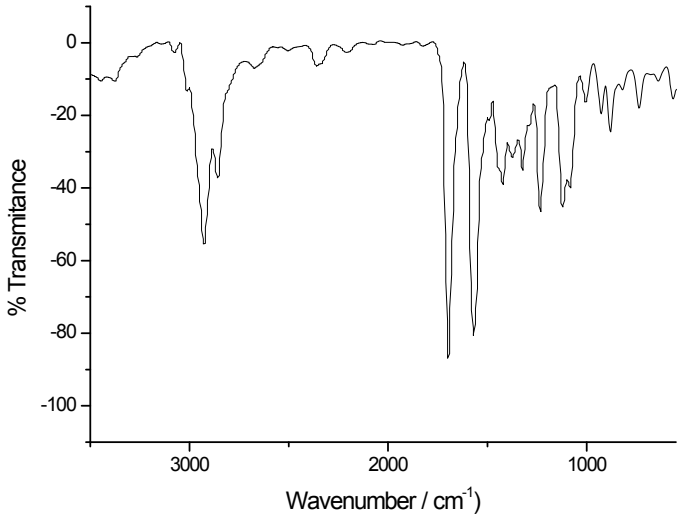

Figure S18. FT-IR spectrum of **smL05**.

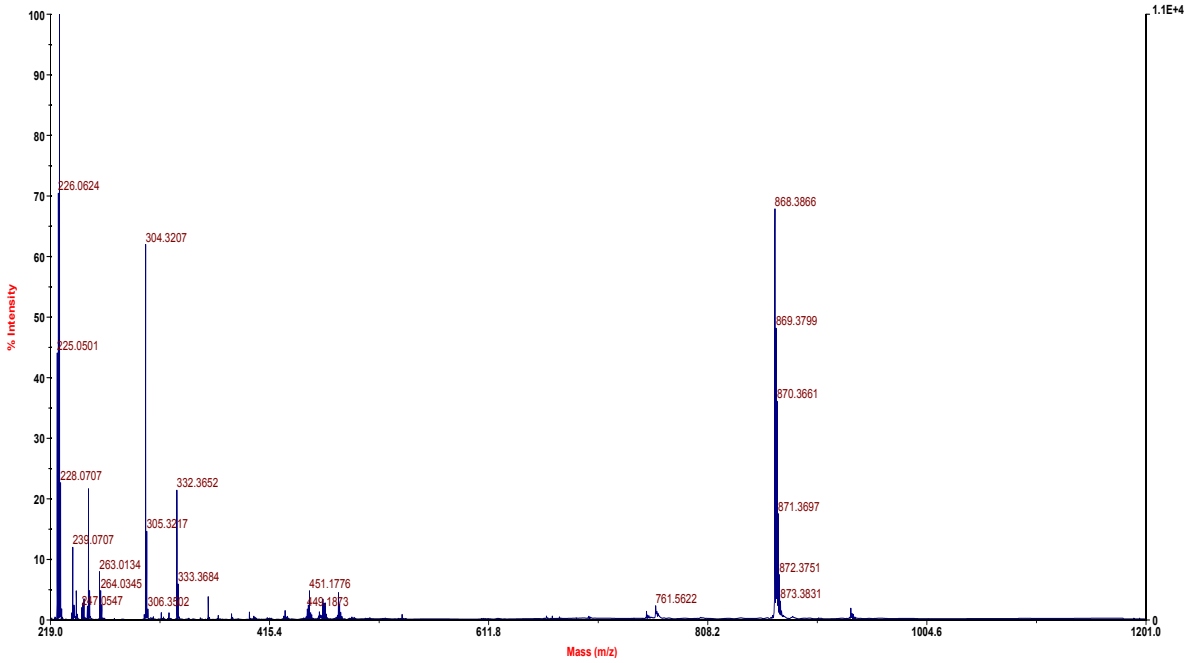

Figure S19. MALDI-MS spectrum of **smL05** (Matrix: Dithranol).

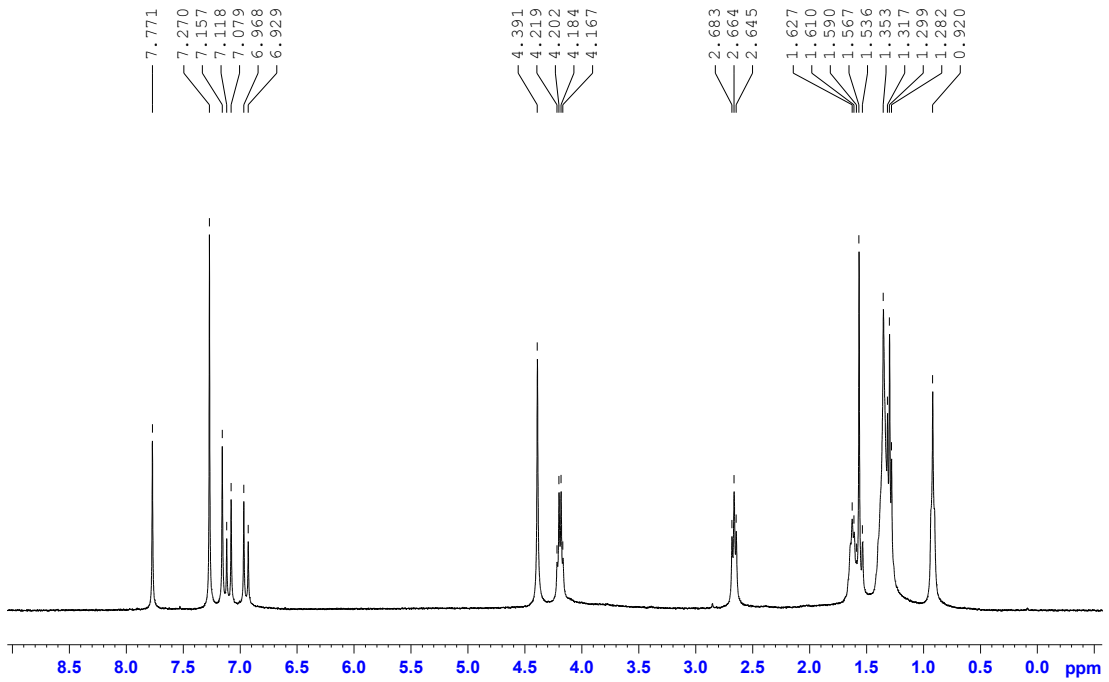

Figure S20. ^{1}H NMR spectrum (400 MHz, $CDCl_3$) of **smL06**.

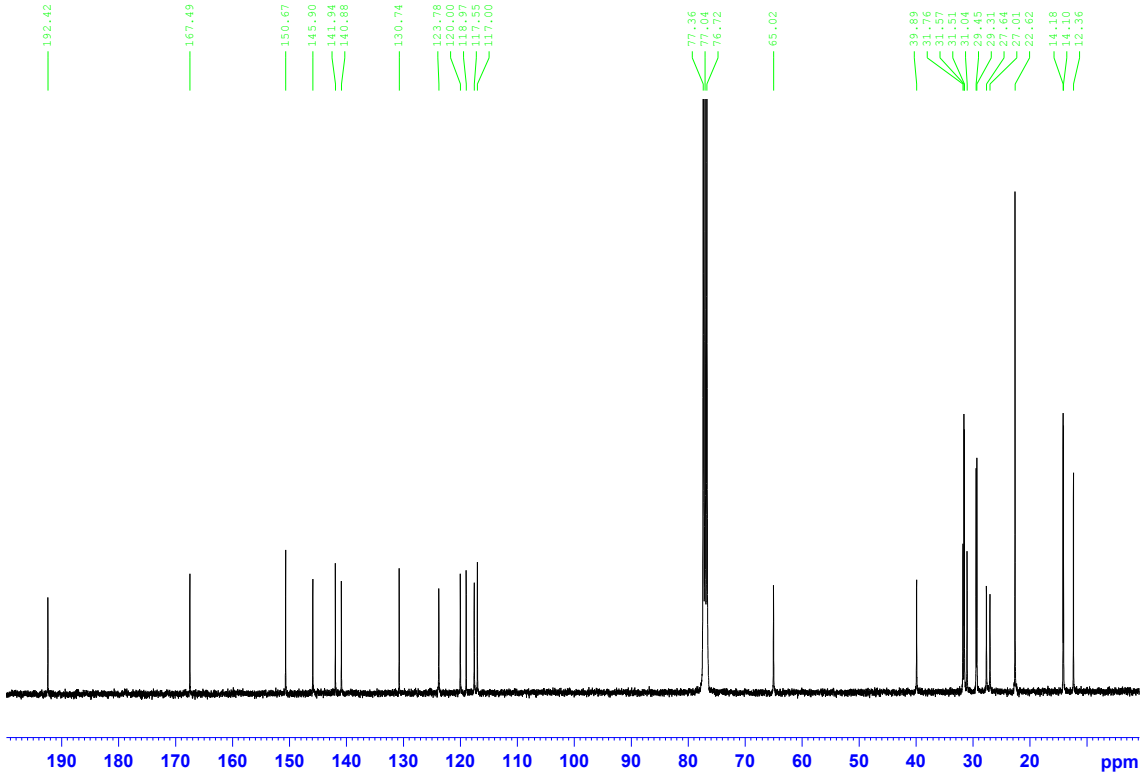

Figure S21. ^{13}C NMR spectrum (100 MHz, $CDCl_3$) of **smL06.**

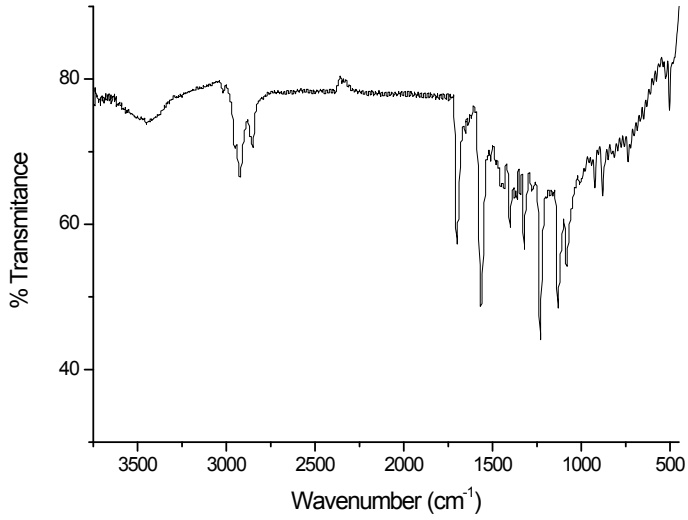

Figure S22. FT-IR spectrum of **smL06**.

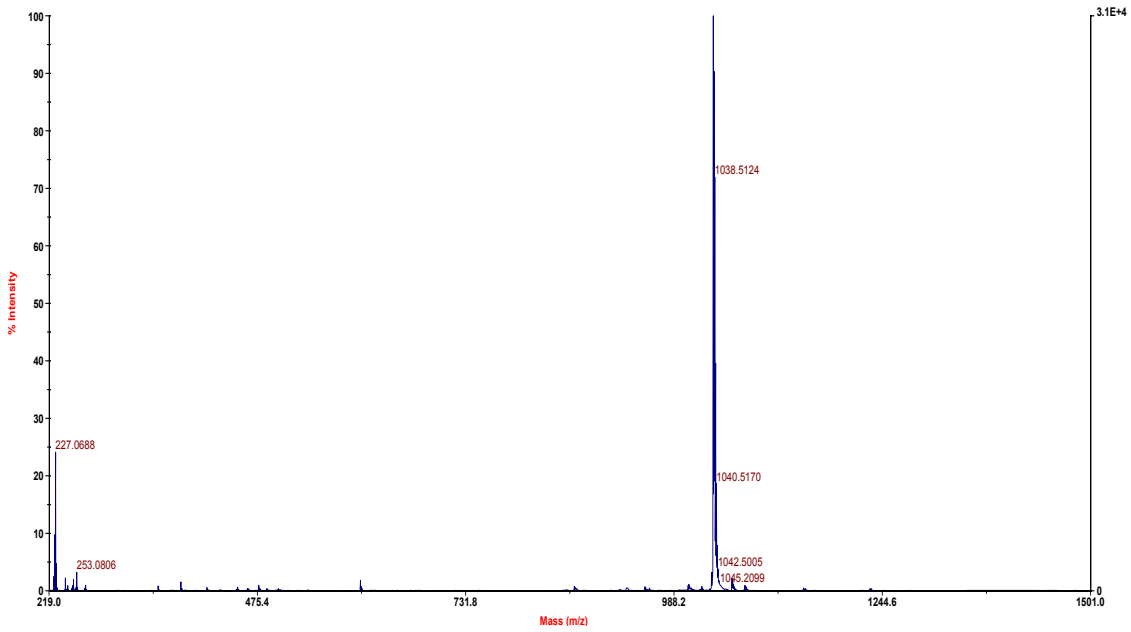

Figure S23. MALDI-MS spectrum of **smL06** (Matrix: Dithranol).

3.- Thermogravimetric analysis of smL04-smL06

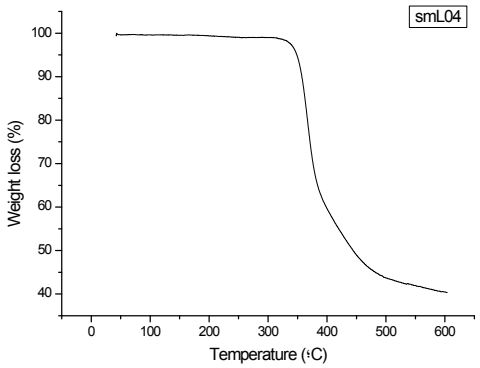

Figure S24. Thermogravimetric analysis of **smL04**.

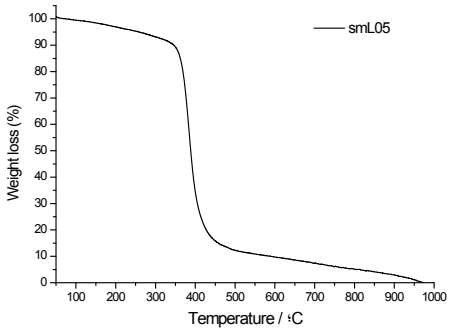

Figure S25. Thermogravimetric analysis of **smL05**.

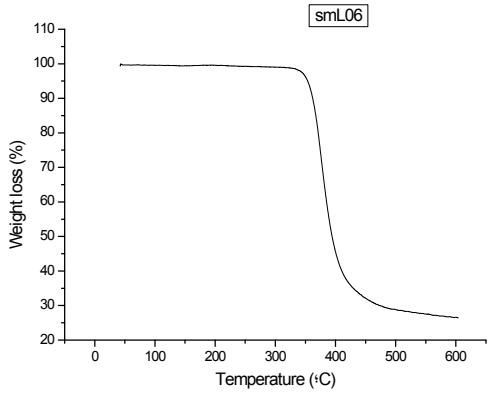

Figure S26. Thermogravimetric analysis of **smL06**.

4.- Differential Scanning Calorimetry (DSC) analysis of smL01 and smL06

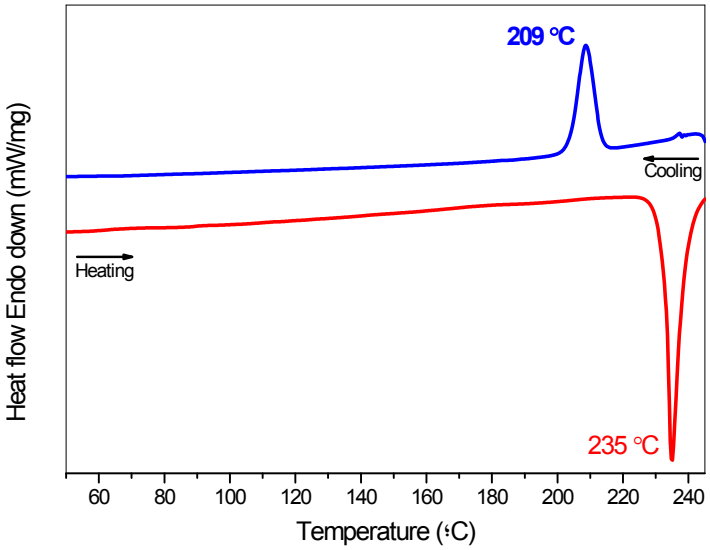

Figure S27. DSC analysis of **smL01**.

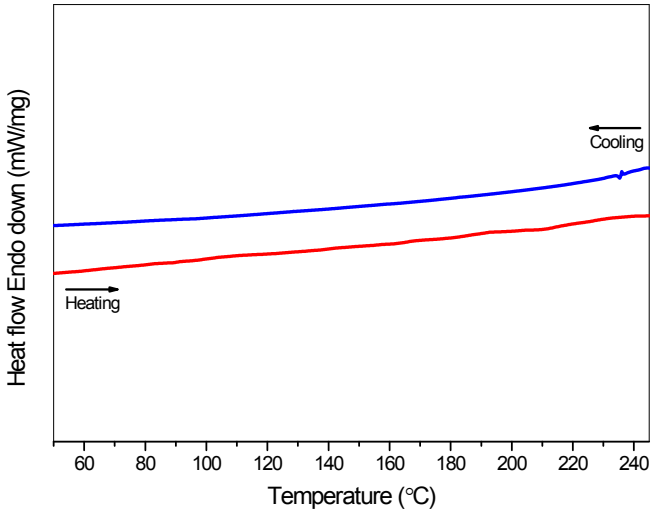

Figure S28. DSC analysis of **smL06**.

5.- Square wave plots of smL01-06.

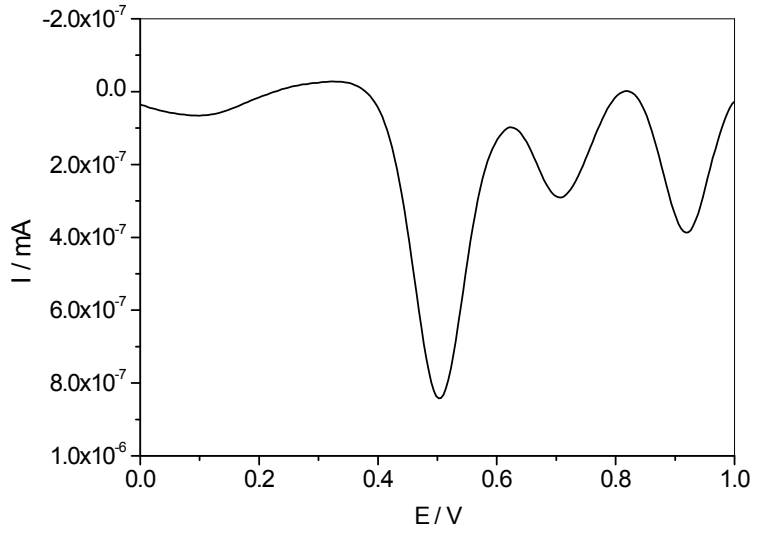

Figure S29. Square Wave Voltammetry plot of **smL01** (referred to Fc/Fc^{+}).

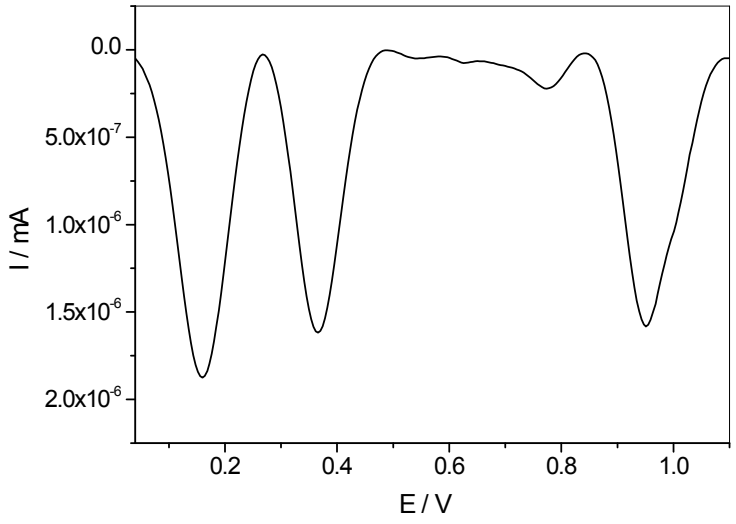

Figure S30. Square Wave Voltammetry plot of **smL02** (referred to Fc/Fc^{+}).

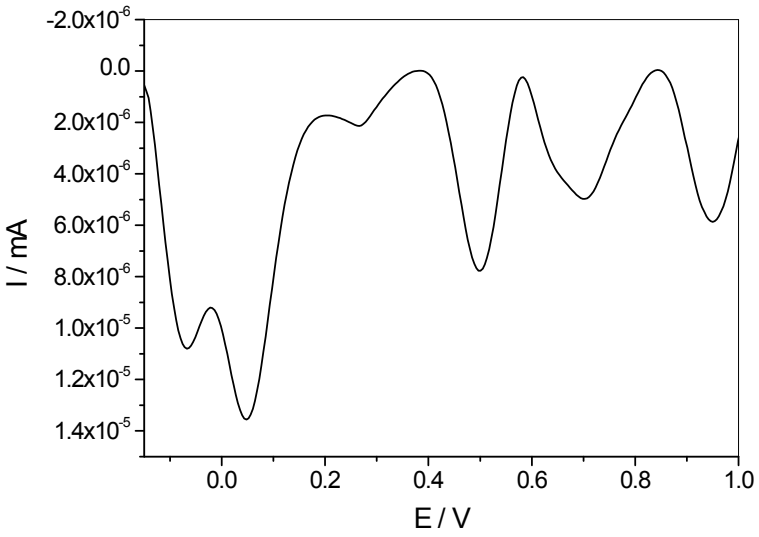

Figure S31. Square Wave Voltammetry plot of **smL03** (referred to Fc/Fc^{+}).

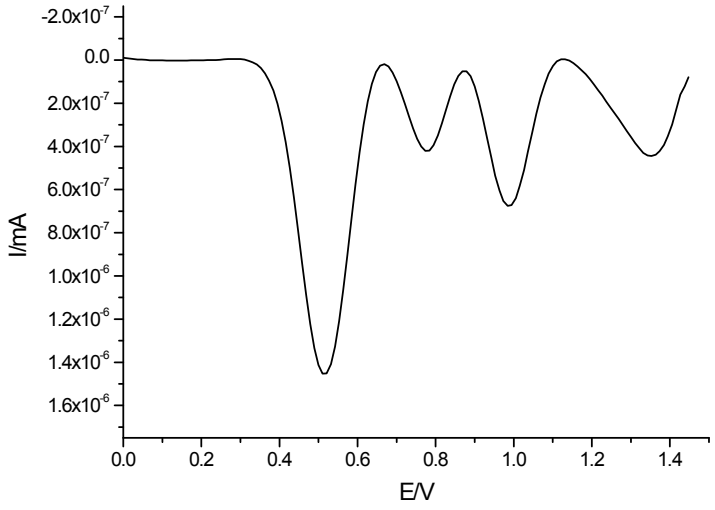

Figure S32. Square Wave Voltammetry plot of **smL04** (referred to Fc/Fc^{+}).

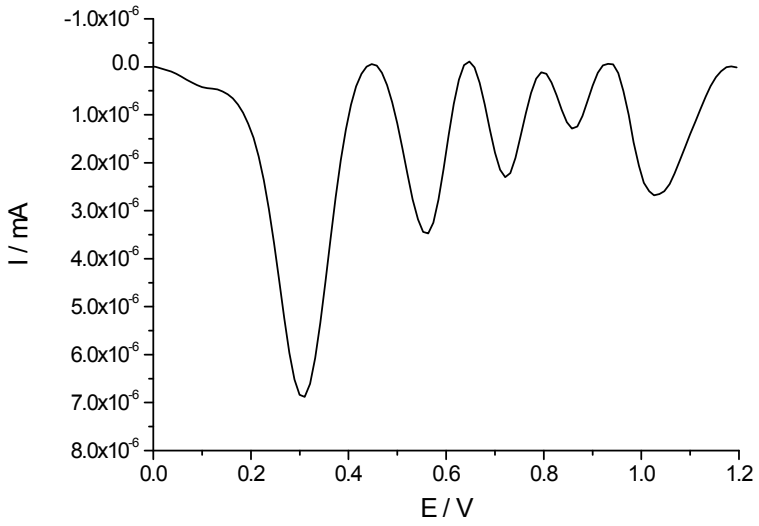

Figure S33. Square Wave Voltammetry plot of **smL05** (referred to Fc/Fc^{+}).

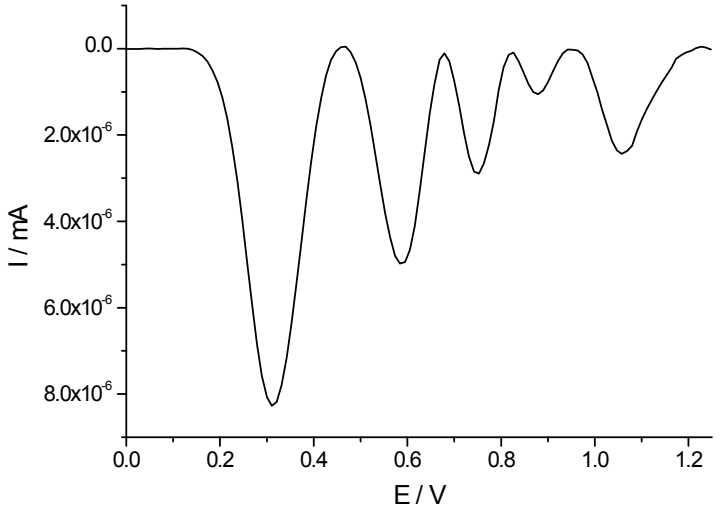

Figure S34. Square Wave Voltammetry plot of **smL06** (referred to Fc/Fc^{+}).

6.- Theoretical calculations.

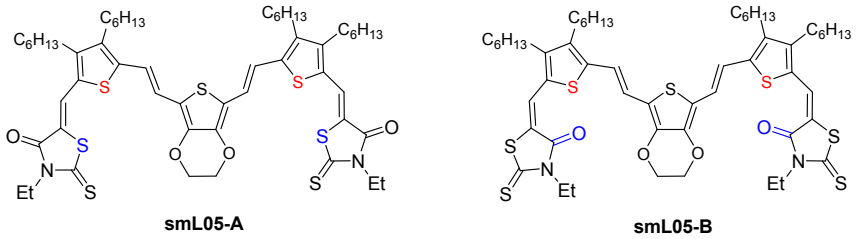

Scheme S1. Possible configurations of **smL05**.

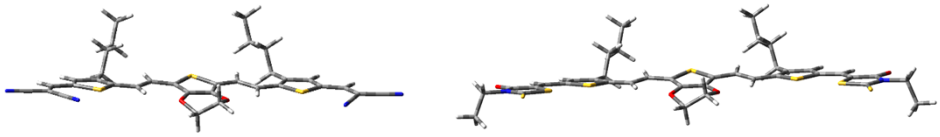

Figure S35. More stable geometries for **smL04** (left) and **smL06** (right).

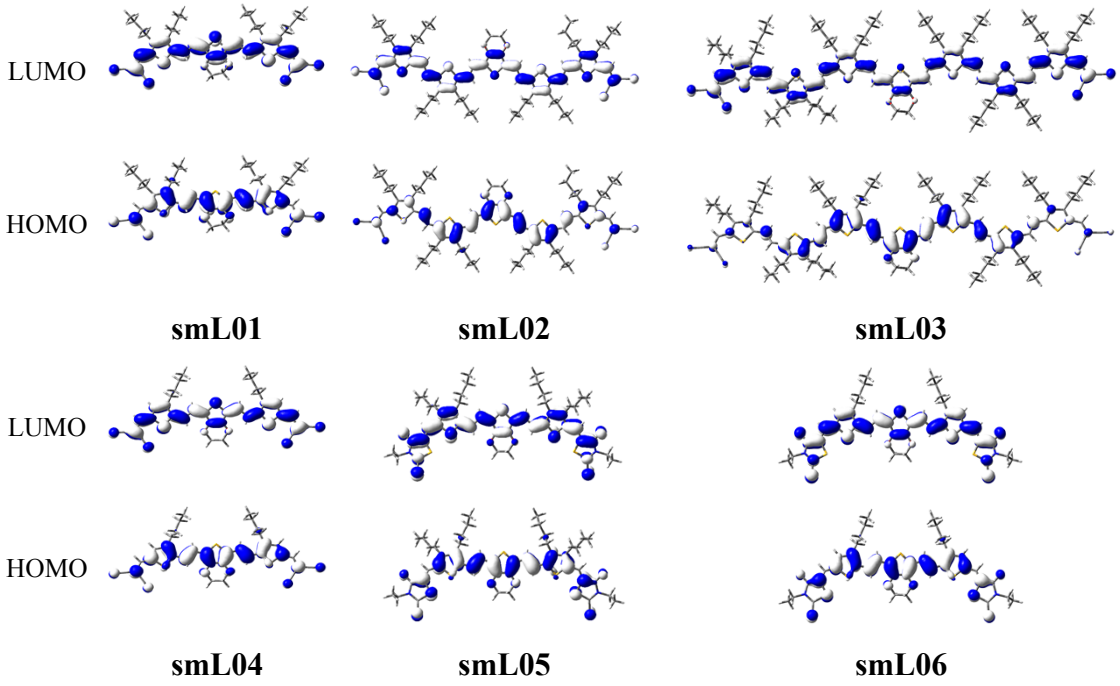

Figure S36. Distribution of orbital coefficients of HOMO and LUMO of compounds **smL01-smL06**.

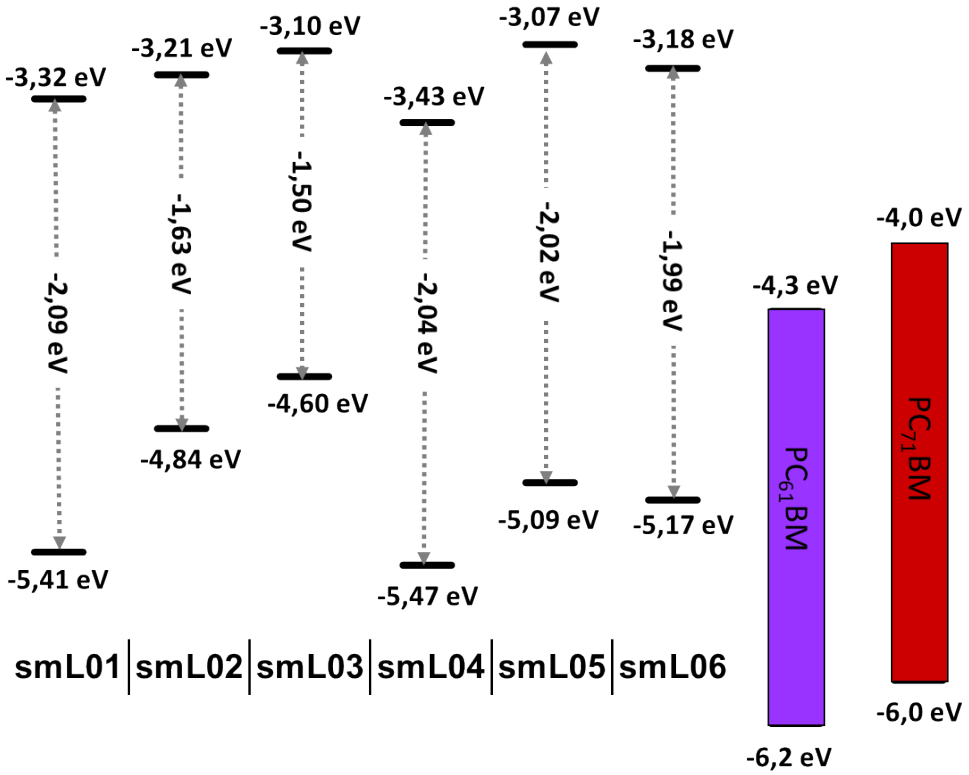

Figure S37. Theoretical HOMO and LUMO energy levels of **smL01-06** related to $PC_{61}BM$ and $PC_{71}BM$.

7.- Absorption spectra of pristine thin films.

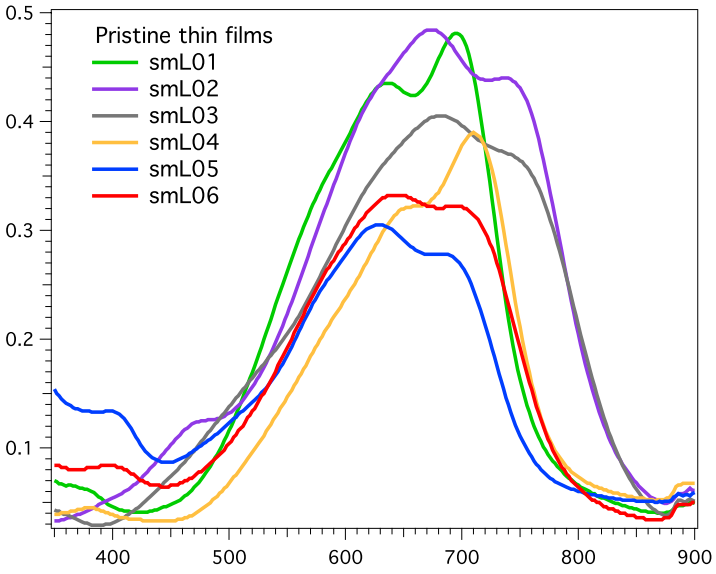

Figure S38. Absorption spectra of smL01-06 pristine thin films using same concentration as in blended films.

8.- Device optimization.

Table S1. Device performance parameters for different optimization processes.

smL01:$PC_{70}BM$ Device characteristics			Device performance parameters			
w/w ratio	**Thickness (nm)**	**SVA time (s)**	**Jsc (mA/cm2)**	**Voc (mV)**	**FF (%)**	**PCE (%)**
1:1	75	0	5.46	1010	63.70	3.51
		60	5.85	1010	63.05	3.85
		180	2.95	989	53.93	1.57
		420	1.07	935	44.26	0.44
	60	60	4.20	1030	60.20	2.61
	100	60	4.36	1020	56.47	2.51
2:1	75	60	3.90	1030	57.93	2.34
1:2	76	60	3.08	1030	51.85	1.57

Table S2. IV performance parameters of optimized **smL:$PC_{70}BM$** complete devices with and without solvent annealing post-treatment.

Device	**J_{sc} (mA cm^{-2})**	**V_{oc} (mV)**	**FF (%)**	**PCE (%)**
smL01 SVA	5.85	1.01	63.70	3.75
smL01 non-A	5.32	984	61.25	3.18
smL02 SVA	3.78	613	66.43	1.54
smL02 non-A	3.08	638	55.67	1.09
smL03 SVA	2.70	562	52.61	0.80
smL03 non-A	2.93	568	51.54	0.86
smL04 SVA	2.50	924	45.43	1.05
smL04 non-A	2.30	914	47.76	1.01
smL05 SVA	4.70	910	34.91	1.50
smL05 non-A	3.85	920	30.34	1.08
smL06 SVA	11.98	890	45.69	4.85
smL06 non-A	4.59	900	32.27	1.33

9.- Mobility measurements.

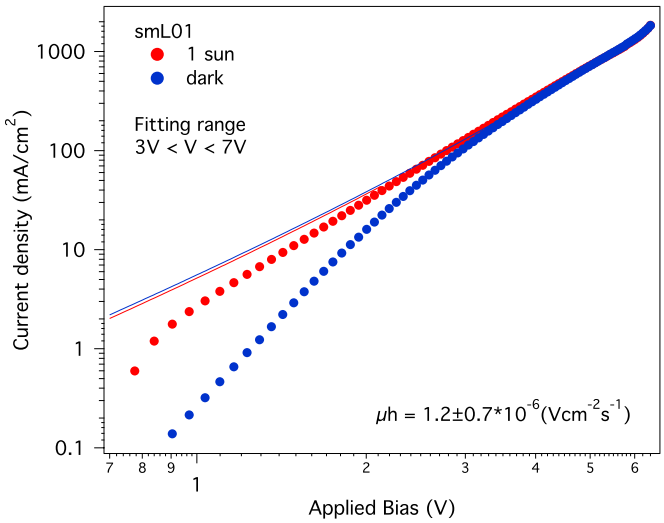

Figure S39. Hole only **smL01**/$PC_{70}BM$ device *I-V* curve at SCLC region.

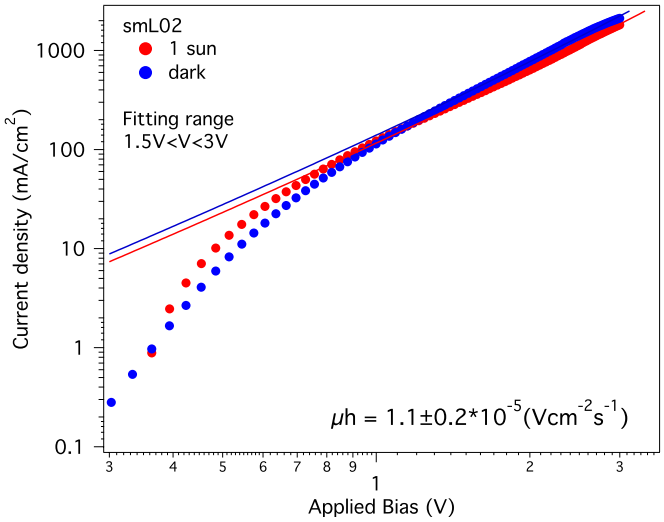

Figure S40. Hole only **smL02**/$PC_{70}BM$ device *I-V* curve at SCLC region.

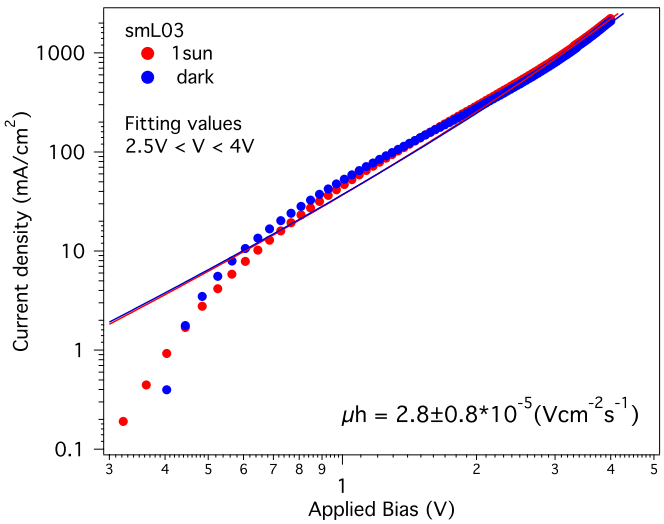

Figure S41. Hole only **smL03**/$PC_{70}BM$ device *I-V* curve at SCLC region.

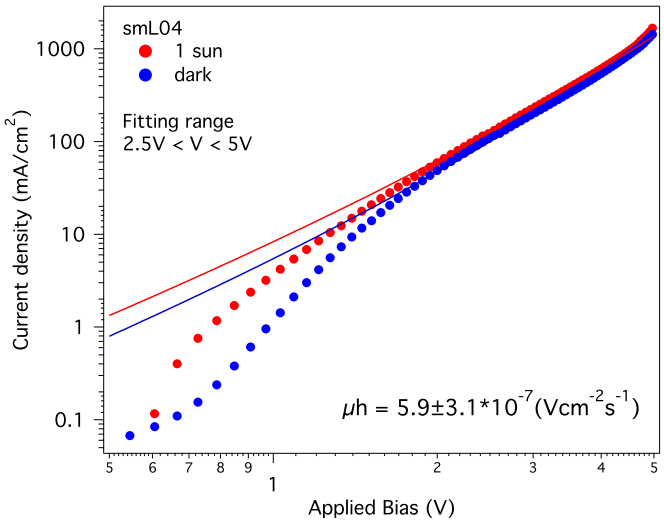

Figure S42. Hole only **smL04**/$PC_{70}BM$ device *I-V* curve at SCLC region.

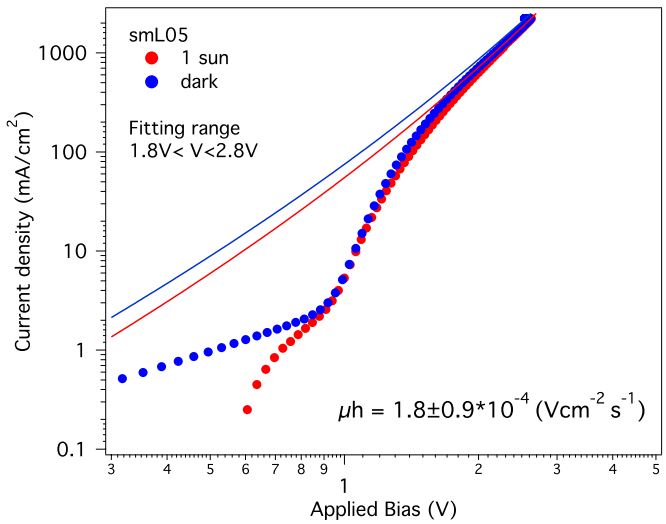

Figure S43. Hole only **smL05**/$PC_{70}BM$ device *I-V* curve at SCLC region.